AIAA JOURNAL
Vol. 44, No. 9, September 2006

Spatial Structure of Cavity Pressure Fluctuations at Transonic Speeds

D. F. Long*
Aero Systems Engineering, St. Paul, Minnesota 55107

DOI: 10.2514/1.5236

Data collected from an axial array of pressure transducers mounted in an open cavity is analyzed using array processing techniques to provide intricate details of the unsteady flow. The wavenumber-frequency spectrum identifies a high frequency–low wavenumber longitudinal standing wave superimposed on the familiar acoustic feedback mechanism. This is shown to be related to the cross stream acoustic mode of the cavity. The pressure field is reconstructed using a shot noise decomposition to identify the temporal evolution. Although the amplitude of the fluctuations can be reduced significantly by leading edge devices, the structural character of the feedback loop and the high frequency standing wave remains constant. When the L/D ratio reduces below 10% the shear layer attaches to the floor and the high frequency standing wave is "cut off". This prevents the upstream propagating acoustic disturbance from reaching the forward wall to complete the cycle.

Nomenclature

a	=	speed of sound
b	=	wavenumber-frequency spectrum
c_j	=	eigenvector
C_p	=	pressure coefficient, p'/q
d	=	cavity depth
$E\{\}$	=	expected value
f	=	frequency
I	=	identity matrix
k	=	wavenumber, $2\pi/\lambda$
K	=	dimensionless wavenumber kL
K_{ij}	=	cross spectral density matrix
L	=	cavity length
M	=	Mach number
M_{ij}	=	modified cross spectral density matrix
n	=	number of sensors
$p(t)$	=	pressure signal
q	=	dynamic pressure
$s(t)$	=	signal component
$S(\omega)$	=	Fourier transform of $s(t)$
Sr	=	Strouhal number, fL/a
t	=	time
t'	=	dimensionless time, ta/L
U	=	freestream speed
U_p	=	phase speed
U_g	=	group speed
x	=	longitudinal coordinate
w_j	=	window function
W	=	cavity width
α	=	event strength
δ	=	Dirac function
λ	=	wavelength
$\lvert\lambda_n\rvert^2$	=	eigenvalue amplitude
τ	=	time lag
ν	=	event rate
ϕ	=	cross spectral density
ω	=	radian frequency
ψ_n	=	continuous eigenfunction

Subscripts

i, j	=	spatial indices
l, n, m	=	subspace indices

Superscript

*	=	conjugate transpose

Presented as Paper 3100 at the 9th AIAA/CEAS Aeroacoustics Conference and Exhibit, Crowne Plaza Resort Hilton Head, SC, 12–14 May 2003; received 31 March 2005; revision received 26 September 2005; accepted for publication 11 March 2006.

*Chief Scientist, Aero-acoustics Division, 358 E. Fillmore Ave, St. Paul, MN; Senior Member AIAA.

Introduction

HIGH speed grazing flow over an open cavity generates intense resonant pressure fluctuations known as Rossiter modes [1]. The conventional interpretation of cavity fluctuations is a propagation/acoustic feedback loop [2,3]. Disturbances created in the initial shear layer convect downstream, grow into turbulent structures, and impact the aft wall of the cavity. Amplification and saturation of the disturbance level results when the noise propagating upstream from this impact event is timed to reinforce the instability of the initial shear layer of the next cycle. The strength of this feedback cycle depends on the transit time of the disturbances in both the downstream and upstream directions. The downstream convection of turbulence in a deep cavity is similar to that for a free shear layer with nominal speed $U_p/U \sim 0.5$. Inside the cavity, below the shear layer, the flow speed is essentially zero and the upstream acoustic propagation speed is $U_p = -a$. Outside the cavity, an acoustic disturbance must travel against the mean flow with propagation speed $U_p = U - a$. In high subsonic flow these speeds are quite different and the feedback structure may be quite different than at low Mach number. As the cavity depth diminishes, several changes to the basic flow pattern are expected. The turbulent convection speed will increase and eventually attain the value for the turbulent boundary layer $U_p/U \sim 0.7$ [4,5]. The impact with the downstream wall will diminish, reducing the intensity of the resulting acoustic disturbance. At zero depth (flat plate solution), the feedback cycle is fully interrupted since the amplitude of the impact disturbance goes to zero. Another means of interrupting the feedback cycle is through modification of the initial shear layer. It is well known that the fluctuation levels in the cavity can be mitigated by installing various devices at the upstream end of the cavity. The mechanism that causes this is unclear. One interpretation is that the small scale turbulent energy created by the device increases the spatial separation from the large resonant cavity scale [6]. Another suggests that the thickened boundary layer modifies the receptivity of the initial shear layer to the

acoustic disturbance. A third suggests that the device simply deflects the shear layer out into the freestream flow enough to reduce the impact at the downstream wall [7].

The present study focuses on the axial variation of the pressure fluctuations within the cavity as a result of changes to three fundamental variables: freestream velocity, cavity depth, and leading edge conditions. The freestream velocity can be continuously varied over the transonic range of interest. The cavity depth is varied in discrete steps using spacers between the flow surface and the floor plate. Three leading edge devices (sawtooth fence, discrete ramps, and transverse blowing) are evaluated and compared with the baseline condition without leading edge modification.

The measurement of interest is the unsteady pressure field along the cavity floor. A row of pressure transducers is installed on the axial centerline along the entire length of the cavity. The data is evaluated using array processing techniques based on the subspace decomposition of the measured cross spectral density. This decomposition was introduced to the turbulence community as the proper orthogonal decomposition theorem (POD) to extract the relevant large scale features of the turbulent velocity field [8]. It has recently been used to generate low dimensional models of the large scale processes from both numerical calculations and experimental measurements in cavity flows [9,10]. The POD decomposition (also known as the Karhunen–Loève expansion) is used as the foundation for two further analyses. The first tool is the subspace wavenumber-frequency spectrum [11]. This provides higher resolution in the spatial statistics than Fourier methods when the number of transducers in the array is low. Spectral peaks are easier to separate and identify with individual flow features. The second tool is a "shot noise" reconstruction using the signal subspace identified from the POD. This produces the most likely signal that is consistent with the measured cross spectrum.

Methods of Analysis

The pressure field is assumed to consist of two components: desirable signals and uncorrelated noise. The signals (fluctuations of interest) can be either acoustic or hydrodynamic and can propagate either upstream or downstream. Noise is uncorrelated with no preferred direction. It may be noise or unsteadiness generated outside of the cavity which impinges on the transducer array. Or it may be uncorrelated fluctuations generated by the cavity itself. The goal is to separate the signal field from the noise field and to determine the spatial structure of the coherent signals.

Several concepts are discussed in the following. The formulation of the cross spectral density matrix (CSDM) is derived. This concept is central to all subsequent processing. This is followed by a discussion of the basic technique for determining the wavenumber of the measurements across the array. This produces the wavenumber-frequency spectrum when applied to the CSDM. It is equivalent to a direct implementation of Fourier methods for the spatial field. Resolution problems are encountered due to the limited number of sensors used in the array. Subspace methods are introduced as a means to improve resolution and optimize the ability of the algorithm to separate closely spaced signals. Strictly speaking, the wavenumber-frequency spectrum is only applicable to cases where the spatial structure of the pressure field is homogeneous. Amplitudes should be similar at each location and phase shifts should be only a function of transducer separation. This ensures that the harmonic functions are the proper basis functions. This requirement is only partially satisfied for the fluctuations within the cavity. The cavity flow consists of a continuous evolution along the length. The unsteadiness at the forward wall is considerably different than that at the rear wall. In these inhomogeneous cases, the proper tool for evaluating the spatial structure is known in the turbulence community as the proper orthogonal decomposition (Karhunen–Loève expansion) theorem. The proper basis functions are a result of the analysis rather than an assumed harmonic form as in Fourier modes.

The processing to be discussed relies on an accurate estimate of the cross spectral density. Formally, this is given by the Fourier transform of the cross correlation function,

$$\phi(x, x'; \omega) = \frac{1}{2\pi} \int R(x, x', t) e^{-i\omega t} \, \mathrm{d}t \tag{1}$$

where $R(x, x', t)$ is the linear correlation,

$$R(x, x', \tau) = \frac{1}{T} \lim_{T\to\infty} \int_0^T p(x, t) p(x', t + \tau) \, \mathrm{d}t \tag{2}$$

describing the expected value of the product between the measurement at x with the measurement at x'. The usual procedure for providing an estimate of $\phi(x, x'; \omega)$ is through the circular correlation resulting from the Fourier transform product,

$$\phi(x, x'; \omega) = E\{P(x; \omega) P^*(x'; \omega)\} \tag{3}$$

where

$$P(x; \omega) = \frac{1}{2\pi T} \lim_{T\to\infty} \int w(x, t) p(x, t) e^{-i\omega t} \, \mathrm{d}t \tag{4}$$

This takes full advantage of the computational efficiency afforded by the fast Fourier transform (FFT). The window function is a necessary component when Fourier transform methods are applied to stationary data to ensure a bounded sum.

Assuming a quasi-homogeneous environment, the spatial structure of the wave field across the array is found from the wavenumber-frequency spectrum. The formal development starts from the basic definition,

$$b(\omega, k) = E\{P(\omega, k) P^*(\omega, k)\} \tag{5}$$

where

$$P(\omega, k) = \frac{1}{(2\pi)^2} \frac{1}{LT} \int_0^L \lim_{T\to\infty} \int_0^T w(x, t) p(x, t) e^{-i(\omega t + kx)} \, \mathrm{d}t \, \mathrm{d}x \tag{6}$$

is the double Fourier transform of the spatiotemporal signal. Equation (6) is substituted into Eq. (5), the exponential is separated, and time is Fourier transformed into frequency, resulting in,

$$b(\omega, k) = \frac{1}{(2\pi)^2} E\left\{ \left[\int P(x; \omega) e^{ikx} \, \mathrm{d}x \right] \left[\int P^*(x'; \omega) e^{-ikx'} \, \mathrm{d}x' \right] \right\} \tag{7}$$

The integration variables x and x' represent separate and independent spatial locations. This feature allows the mean square formulation to be rearranged and the expected value operator to be taken inside the integrals

$$b(\omega, k) = \frac{1}{(2\pi L)^2} \int_0^L \int_0^L e^{ikx} \phi(x, x'; \omega) e^{-ikx'} \, \mathrm{d}x \, \mathrm{d}x' \tag{8}$$

where ϕ is given by Eq. (3). Equation (8) is the functional form of the wavenumber-frequency spectrum. The axial wavenumber k is the spatial transform of the location vector x. The output $b(\omega, k)$ is real valued and represents the power in a two-dimensional bandwidth contained within $\mathrm{d}\omega$ and $\mathrm{d}k$.

Because an approximation using discrete probe locations is necessary, the vector representation of Eq. (8) becomes

$$b(\omega, k) = \sum_{j/l=1}^{n} [w_j(\omega) e^{ikx_j}] K_{jl}(\omega) [w_l(\omega) e^{-ikx_l}] \tag{9}$$

The quantity inside the square brackets is the projection (or steering) vector; the exponential terms provide the distribution of sinusoidal energy at a particular ω across the wavenumber band. The spatial weighting coefficient $w_j(\omega)$ includes the constant factors in Eq. (8) and represents the spatial window through which the data is viewed at each frequency. The weighting coefficient has the form $w_i = D_{ij}\beta_j$. β is the weight imposed on the problem according to the particular algorithm. D is the quadrature that best represents the discrete version of the implied integration. The present study uses an equally spaced array with a boxcar data window and the weighting

function becomes $\delta_{ij}d/n$. The formulation for nonuniform arrays is taken up elsewhere [11]. In either case, the weighting function has the effect of converting the measured matrix K into a new matrix M.

The standard estimate [Eq. (9)] determines the wavenumber spectrum of the spatial field by Fourier methods. In the time domain, Fourier methods provide an adequate description because sufficient record length is normally available through digital sampling and ensemble averaging. Spatial data, however, is limited by the number of transducers available and resolution problems are expected when Eq. (9) is applied to data. Adaptive methods are used to improve the resolution of the basic estimate. The concept is to choose the weighting coefficients in an optimal sense based on the data. The weighting coefficients adapt or change according to a prescribed rule as the data changes. The concept was first presented in the context of geophysical data [12]. It was formulated as a variational problem: minimize the energy away from the specified wavenumber (or away from the "look" direction using beamforming terminology) while maintaining unity gain overall. This method is currently known as maximum likelihood spectral estimation [13]. The result is

$$b(\omega, k) = [e^{-ikx_j}(M_{jl})^{-1}e^{ikx_l}]^{-1} \tag{10}$$

which conveniently avoids explicit reference to the weighting coefficients. The interpretation associated with the improved estimate in Eq. (10) is opposite to that for the direct method. The direct method [Eq. (9)] seeks to maximize the projection of the data onto an assumed sinusoidal waveform. The improved method [Eq. (10))] seeks the signal components as the inverse of the "noise." Signals are the prominent feature of the original CSDM; noise is the prominent feature of the inverted matrix. This concept is considered further in the subsequent discussion on subspace methods.

Subspace filtering provides further analysis of the pressure field across the array. This procedure is relatively common in fields such as radar and sonar, going by either subspace methods or by an eigenvalue analysis. The individual components of the unsteady signal are separated into distinct orthogonal spaces via the Karhunen–Loève expansion. The basis of the expansion interpreted in terms of the pressure signal states that the spatial pressure signal $p(x)$ has an orthogonal decomposition

$$p(x) = \sum_n \lambda_n \xi_n \psi_n(x) \tag{11}$$

with

$$E\{\xi_n, \xi_m\} = \delta_{nm}, \qquad \int \psi_n(x)\psi_m(x)\,\mathrm{d}x = \delta_{nm}$$

if, and only if, the λ^2 are the proper values and the ψ are the proper functions of its covariance [14]. The nature of ξ is not known explicitly but its integral properties described by Eq. (11) indicate that the formulation is based on second order statistics and that multiple ensembles are needed to minimize uncertainty. An individual realization of the measured signal is not required to conform to any components of the sum, but on average, the mean square energy in the measured signal is properly represented in the decomposition. The proper values and proper functions (hereafter called eigenvalues and eigenfunctions) represent the decomposition of the wave field in the array direction into orthogonal components and are found from the solution to the equation

$$\int R(x, x', \tau)\psi_m(x', \tau)\,\mathrm{d}x' = |\lambda_m(\tau)|^2\psi_m(x, \tau) \tag{12}$$

where $R(x, x')$ is the covariance of the pressure signal defined in Eq. (2).

Stationarity in time implies that a Fourier transform may be used to decompose the time signal into orthogonal components since it is known that the proper basis functions of a stationary field are the harmonic functions. Thus, using Eq. (1), Eq. (12) can be transformed into

$$\int \phi(x, x'; \omega)\psi_m(x', \omega)\,\mathrm{d}x' = |\lambda_m(\omega)|^2\psi_m(x; \omega) \tag{13}$$

The kernel ϕ in this equation is the cross spectrum and is identical to the quantity in Eq. (3). The subscript m stands for an infinite and continuous spectrum of solutions for which λ^2, the eigenvalue, is real and represents energy content. The eigenfunction ψ represents the basis function, orthogonal to all other basis functions.

The matrix equivalent to Eq. (13) using discrete probe locations is

$$K_{ij}D_{jk}C_k^m = |\lambda_m|^2 C_i^m \tag{14}$$

C is the discrete version of the eigenfunction $\psi(x)$ and D is the quadrature integration matrix. With equal probe spacing and a diagonal integration matrix D_{ij}, the product matrix $[K][D]$ is Hermitian, with the immediate implication that the eigenvalues are real valued as required by the continuous formulation. This simplification is assumed in the remainder. Systems with more complex integration or nonequal transducer spacing can also be used but require additional manipulation to create a Hermitian matrix [11]. Equation (14) defines a matrix eigenvalue problem that is solvable by standard techniques in linear algebra. As many eigensolutions can be computed as the rank (size) of the matrix, each in decreasing energy. If a single eigenvalue dominates the solution then the field is associated with a single structure. If multiple eigenvalues of sufficient energy are present then energy is associated with multiple structures.

The CSDM can be separated into

$$K_{ij} = \sum_{m=1}^{k} |\lambda_m|^2 C_i^m C_j^{m^*} + \sum_{m=k+1}^{n} |\lambda_m|^2 C_i^m C_j^{m^*} \tag{15}$$

The first term, consisting of k components, is the signal subspace. The second term, consisting of the remaining components, is the noise subspace. If the noise is perfectly uncorrelated the second term becomes $|\lambda|^2 I$, but real data requires the formulation in Eq. (15). Mathematically, this division can be determined as the amount of energy that can be removed from the main diagonal of the CSDM that retains the matrix as positive definite [15]. In practice, however, it is usually easier to choose the value of k from experience.

The subspace wavenumber-frequency spectrum is found by operating on the noise subspace in Eq. (15). A reconstructed matrix of the form

$$M_{ij}^{-1} = \sum_{m=n}^{k+1} a_m C_i^m C_j^{m^*} \tag{16}$$

is used in Eq. (10). The sum is taken in reverse order from Eq. (15) and the coefficients a_m are the inverted eigenvalues. This "adaptive-eigenvector" method assumes that the n–k noise subspaces have been identified. Sometimes, instead of coefficients equal to the inverted eigenvalues, the noise subspaces are normalized by giving equal weight to each individual noise subspace. This is known as the multiple signal classification (MUSIC) algorithm [13]. The matrix reconstructed from Eq. (16) with $a_m = 1$ whitens the noise field that is orthogonal to the signals, sometimes producing a clearer representation of the spectrum.

A representative spatiotemporal signal (or shot) can be reconstructed using the signal subspace identified in Eq. (15). The shot effect assumes that the measured signal is composed from a sequence of similar random overlapping events [16]. This procedure defines the inverse Fourier transform of the spectrum associated with the signal subspace as a "characteristic eddy" [8]. In the present case, the characteristic structure (x–t event) of the signal subspace can be reconstructed from the inverse Fourier transform of the measured spectrum. A signal spectrum is defined using the signal subspace

$$S_i(\omega) = \sum_{n=1}^{m} \lambda_n C_i^n(\omega) \tag{17}$$

The inverse Fourier transform of Eq. (17) leads to the best estimate of

the coherent temporal signal at the ith transducer location

$$(\alpha^2)^{\frac{1}{2}} s_i(t) = \int S_i(\omega) e^{i\omega t}\, \mathrm{d}\omega \tag{18}$$

The multiplier α is a strength function which defines the unknown amplitude of the characteristic signal. Its value depends on the average rate of occurrence. The event could be violent but rare, or it could be frequent and far less energetic. Unfortunately, second order statistics in the CSDM are insufficient to solve this issue. The method of moments in the form expressed as Campbell's theorem is used to find the rate of occurrence by relating the fourth moment of the data to the fourth moment of s_i [16]. Accounting for the energy balance between the data and the characteristic signal leads to the rate of event occurrence

$$\nu_i \sim \frac{\overline{(p'^2)}^2}{p'^4} \frac{\int_{-\infty}^{\infty} s_i^4(t)\, \mathrm{d}t}{\left[\int_{-\infty}^{\infty} s_i^2(t)\, \mathrm{d}t\right]^2} \tag{19}$$

The first term is the inverse kurtosis of the measured data. The ratio of the two integrals is the kurtosis of the reconstructed signal. The relationship between these two quantities defines the rate of occurrence.

To summarize, two analytical tools will be used to evaluate the spatial structure of the pressure fluctuations within the cavity. Both are subspace methods based on the eigendecomposition of the CSDM. Three versions of the wavenumber-frequency spectrum are considered. The standard version, determined through Eq. (9), seeks to maximize the projection of the data onto an assumed sinusoidal wave form. The adaptive maximum likelihood version seeks to maximize the noise rejection, thereby retaining the signals. This is determined through Eq. (10). The subspace version of the wavenumber-frequency spectrum takes the noise rejection concept one step further. Instead of inverting the matrix to make the noise components prominent, the matrix is separated formally into signals and noise. Equation (15) performs the subspace separation, Eq. (16) reconstructs the matrix from the noise subspace, and the reconstructed matrix is inserted into Eq. (10). The procedure is applied to the forward and rear parts of the cavity separately where quasi-homogeneous conditions exist. This identifies the approximate size and speed of the structures in each half of the cavity. The second tool is the shot effect reconstruction of the data. It operates directly on the signal subspace in Eq. (15) using Eqs. (17–19). This is deemed to be the most likely event that is consistent with the measured CSDM.

Experimental Setup

Wind tunnel tests are performed in a 56×56 cm transonic wind tunnel shown in Fig. 1. This is an induction wind tunnel where flow is established using high pressure air ejectors downstream of the test section. The facility is configured to minimize the upstream propagation of noise from the model support region and the ejector drive system which may otherwise hinder the measurement of the cavity pressure fluctuation levels. Evaluating the wavenumber-frequency spectrum for the clean tunnel identifies the background noise and unsteadiness associated with the wind tunnel. In all cases considered here the background noise is more than 10 dB below the cavity fluctuations of interest.

Fig. 1 Transonic wind tunnel (test section sidewall open).

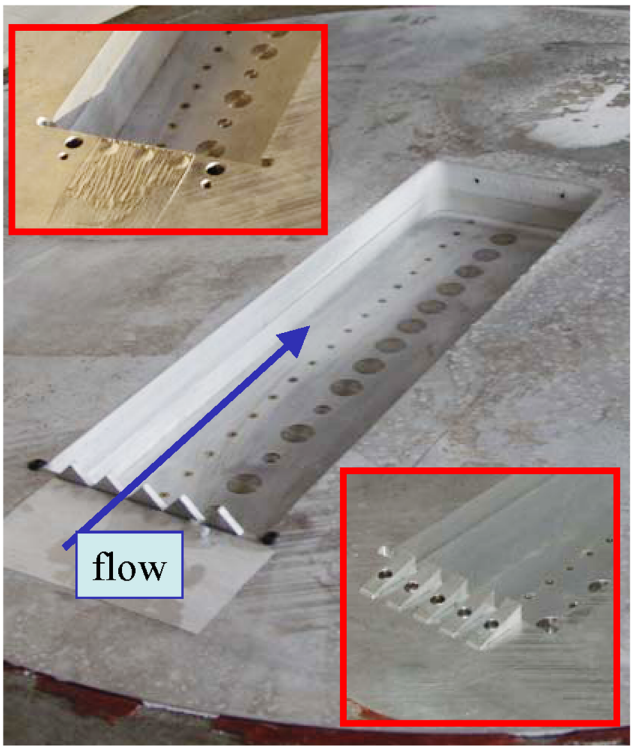

Fig. 2 Cavity model.

The model shown in Fig. 2 is installed into the floor of the wind tunnel. It is 75 mm wide and 250 mm long. The depth can be varied from 12 to 41 mm using interchangeable spacers between the flow surface and the floor. The configuration shown has a depth of 22 mm. This shows the leading edge (LE) devices used in this study. The main image shows a sawtooth fence. The lower inset shows a row of discrete ramps. Both of these devices protrude from the surface by 6 mm which is $\sim$ one boundary layer displacement thickness δ^*. The upper inset shows a pair of air injection holes set to produce a flow rate equivalent the mass deficit from the displacement thickness $WU\delta^*$. The cavity floor shows the location of the flush mounted pressure transducers and a row of pressure taps to measure the static pressure distribution. The transducers are PCB model 106B, which have a signal sensitivity of 0.04 mV/Pa and a frequency cutoff of approximately 15 kHz. The spectral content is identified using a fast Fourier transform routine (FFT) to produce the cross spectral density matrix. The final spectral density matrix for a given test point results from ensemble averaging over several data bursts.

Experimental Results

The baseline conditions for these tests are $M = 0.85$ and $d = 41$ mm. Variations on these parameters will be compared with the baseline. The overall behavior of the pressure field within the cavity is presented in Figs. 3 and 4. The static pressure rise on the cavity floor indicates an adverse pressure gradient as the flow approaches the rear wall of the cavity. A similar increasing level is seen in the dynamic pressure. The leading edge devices cause a reduction in both the static and dynamic pressure and the fence causes the largest change from the clean condition in both parameters.

The dynamic data is processed into the cross spectral density matrix to define the amplitude and phase shift for every transducer

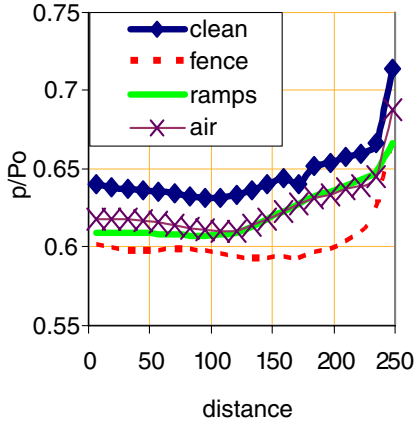

Fig. 3 Static pressure along cavity floor; $M = 0.85$, $d = 41$ mm.

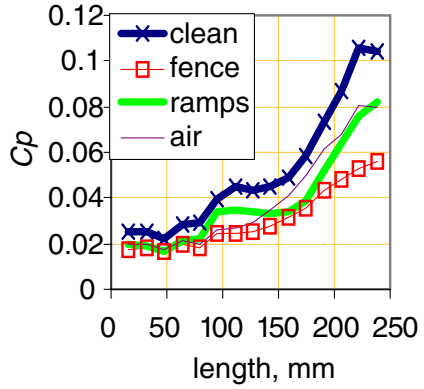

Fig. 4 Dynamic pressure along cavity floor; $M = 0.85$, $d = 41$ mm.

pair. An example of the CSDM is shown in Fig. 5. Part a shows the amplitude along the main diagonal (i.e., power spectra) and part b shows the phase for several transducer pairs. The legend denotes the transducer locations starting at the rear and progressing forward. The amplitude spectra behave similarly to the overall C_p level shown on Fig. 4. The highest fluctuation level is at the rear of the cavity and there is clear indication of the resonant Rossiter modes. However the phase spectra are considerably more random. There is no obvious trend as there is with the amplitude spectra. Inspection of the off-diagonal amplitude terms can provide insight into which transducer pairs are most important, but the problem quickly becomes unwieldy as more and more transducer pairs must be considered. Processing the cross spectra using the rigorous and unbiased approach provided by the subspace methods presented previously eliminates the need to rationalize the meaning of the individual curves of the spectrum. As long as there are sufficient ensembles the matrix will be full rank. This ensures that the matrix is nonsingular and can be decomposed into the subspaces through Eq. (15). Further operations on either subspace are then possible. This provides a considerably clearer picture of the structural features than can be deduced directly from the CSDM.

Figure 6 shows an example of the eigenspectra (energy content) for several subspaces. The sum of the power spectra at each frequency represents the total energy. The sum of all the eigenvalues must equal this total. This clearly shows that the first few eigenvalues contain most of the energy and the dominant eigenvalue contains nearly all of the energy in the resonant spikes. This chart allows the proper value of k in Eq. (15) to be chosen.

For historical reasons derived from bearing detection in radar and sonar applications, the wavenumber spectral procedures are known as beamformers. When a propagating wavefront arrives on the array, the wavenumber can be uniquely related to the frequency via a dispersion relation and a fixed and known propagation speed. Deviations between the measured speed across the array and the

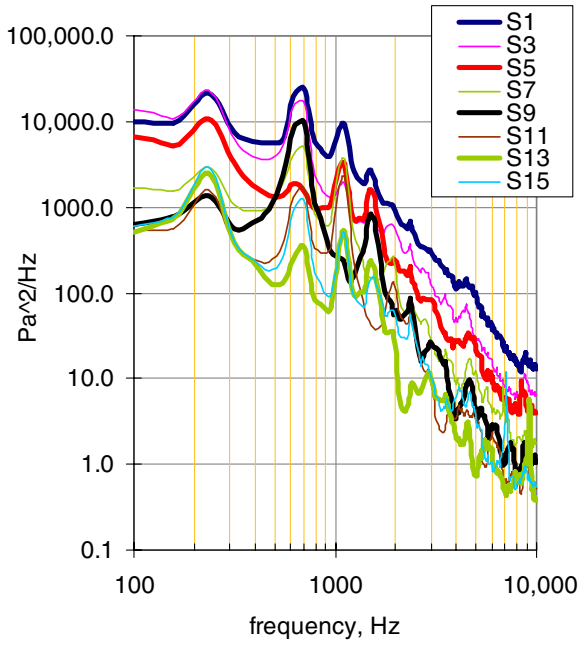

a) amplitude

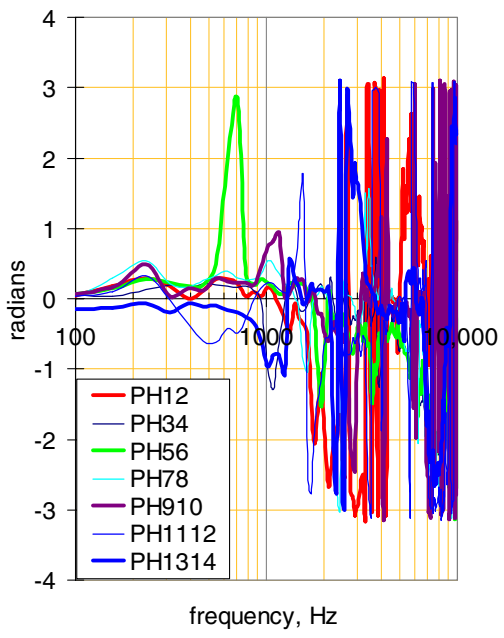

b) phase

Fig. 5 Baseline cross spectral density; $M = 0.85$, $d = 41$ mm.

known propagation speed can be identified with a source or beam direction. This terminology is retained for the subsequent discussion.

The three beamformers are compared in Fig. 7 using data from an eight element array in the downstream half of the cavity. Each procedure captures two peaks. The conventional method known as the frequency domain beamformer (FDBF) results from Eq. (9). This is equivalent to a direct application of the Fourier transform applied to the spatial data. This unitary transformation ensures that the integral across the range of wavenumbers ($|k| < \pi/d$) equals the spectral energy for the frequency in question. The maximum likelihood spectrum (also known as the minimum variance distortionless look, MVDL) beamformer results from Eq. (10). The MUSIC beamformer results from the matrix reconstruction in Eq. (16) with $k = 4$ and $a_m = 1$. Both of these formulations are not true spectra as they are not unitary transformations. Their goal is to improve the resolution and identify the location of spectral peaks, not to conserve the energy content. The MVDL uses variable weighting

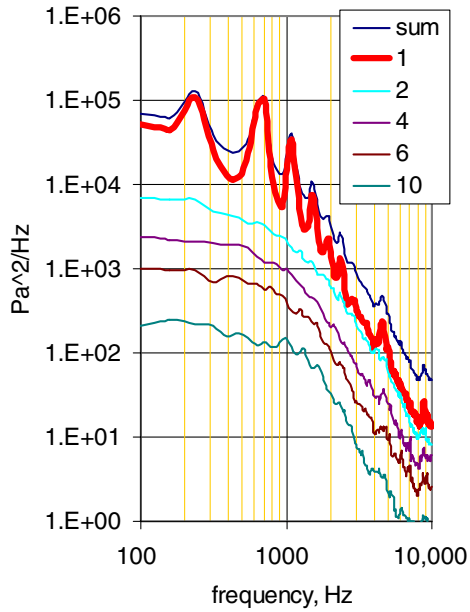

Fig. 6 $|\lambda|^2$ spectrum; $M = 0.85$, $d = 41$ mm, clean LE.

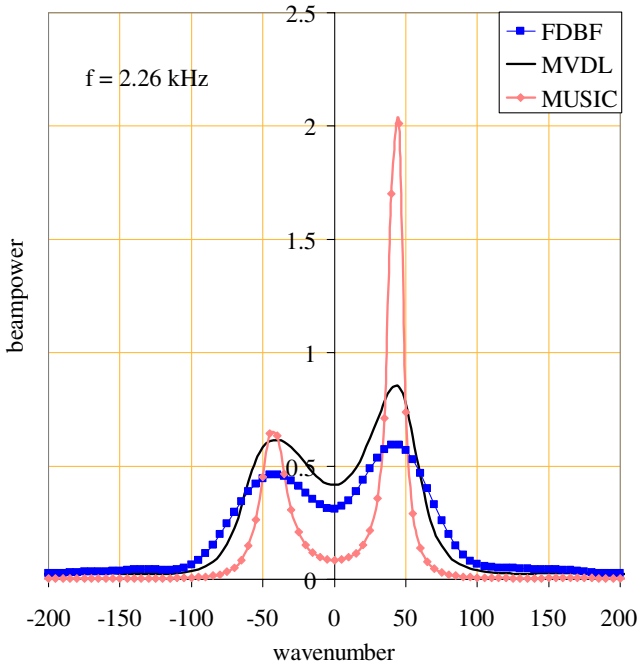

Fig. 7 Example wavenumber spectra.

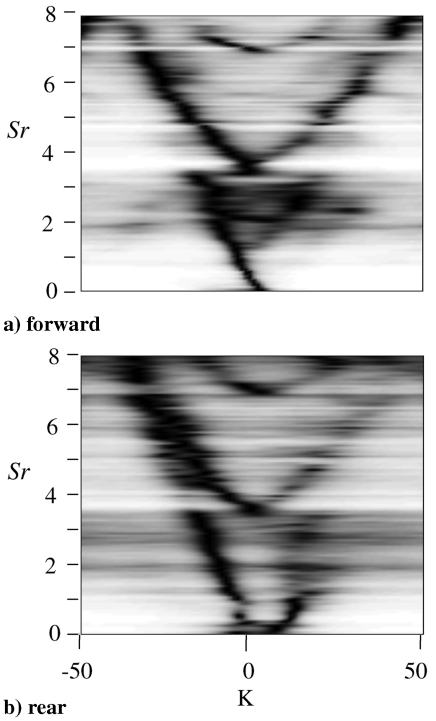

Fig. 8 ω–k spectrum; $M = 0.85$, $d = 41$ mm, clean LE.

coefficients to improve resolution. This results in spectral peaks which bear the same amplitude in relation to each other as in the FDBF but the integral nature of the spectrum is not conserved. The MUSIC spectrum loses amplitude information entirely and merely identifies the distinct subspaces.

The subspace method described in Eq. (16) is used in the remainder of this discussion. Each array consists of eight elements in either the forward half or the rear half of the cavity. In all cases, the value $k = 4$ is used in Eq. (16) to divide the signal and noise subspaces. Higher or lower values do not significantly alter the character of the results. The complete wavenumber-frequency (ω–k) spectrum is constructed by successive application for each frequency component. Because of the wide dynamic range between low frequencies and high frequencies, the ω–k plots are normalized by the maximum value at each frequency. Thus, these spectral plots should only be used to identify characteristics. Evaluation of energy content must be referred to the frequency spectrum.

Figure 8 shows the baseline ω–k spectrum for the fluctuations on the cavity floor. Dimensionless units are used for these spectra. The Strouhal number ($0 < Sr_L < 8$) and the dimensionless wavenumber ($|K| < 50$) are defined in the nomenclature. Note that $Sr_L = 1$ or $K = 2\pi$ corresponds to an acoustic wavelength equal to the cavity length and $Sr_L = 3.3$ or $K = 6.6\pi$ corresponds to an acoustic wavelength equal to the cavity width. These are key parameters which separate the different fluctuating modes. The charts define the wave propagation characteristics. Positive wavenumbers correspond to downstream propagation and negative wavenumbers correspond to upstream propagation. Structural features that appear to radiate from the origin have a constant phase velocity defined as $U_p = \omega/k$. These are termed nondispersive waves; all Fourier components travel at the same speed. Structural features that do not radiate from the origin but nevertheless appear as straight lines have a constant group velocity $U_g = \mathrm{d}\omega/\mathrm{d}k$. These waves are also nondispersive and define a wave packet which consists of a group of Fourier modes. The group velocity describes the speed of a wave group whose individual components travel at different speeds. Some components travel faster than the group and overtake the slower components. The group can still be identified as a distinct structural entity that changes shape as it travels from its origin to its demise. Structural features that curve have a nonconstant group velocity and are called dispersive waves. The components of each wave packet not only travel at different speeds but also change amplitude. A symmetric, or nearly symmetric, arrangement suggests a standing wave field. These definitions allow proper interpretation of the spectral charts.

Figure 8 shows a noticeable difference between the forward and rear portions of the cavity but the structural elements are similar. Both sets can be divided into four distinct frequency regions. Region 1 ($Sr_L < 1$) is dominated by downstream propagation in the rear half of the cavity and upstream propagation in the forward half of the cavity. Region 2 ($1 < Sr_L < 3.5$) shows upstream propagation in both sections of the cavity at a nominally constant phase speed $\sim -a$. Region 3 ($3.5 < Sr_L < 7.0$) shows a symmetric pattern indicating a high frequency standing wave field. The group speed is nearly constant and the upstream mode is slightly stronger. The apex of this structure at $Sr_L \sim 3.5$ (4.5 kHz) corresponds exactly with the small but noticeable spike in dominant eigenspectra in Fig. 6. It is also evident in the standard spectra in Fig. 5 on some of the individual transducers but would be difficult to identify as a distinct entity by

direct inspection. This is the cutoff frequency for the fundamental cross-stream duct mode $\lambda = W$. The fact that this frequency corresponds to $k = 0$ clearly identifies this as a long wavelength longitudinal structure related to the fundamental cross-stream mode. The fluctuations are fully correlated over the entire length of the cavity which may suggest how high frequency information is transmitted between the turbulent impact on the downstream wall and the initial shear layer at the upstream wall. Region 4 ($Sr_L > 7.0$) also contributes to this process as a harmonic of region 3 owing to the similar character at twice the frequency.

Figure 9 shows the characteristic x–t event derived from Eqs. (17–19) for the same conditions as in Fig. 8. The amplitude scale is given in terms of $C'_p = p'/q$. The horizontal axis marks the distance from the cavity leading edge, and the vertical axis defines the evolution with time $t' = tU/L$. The range extends from $-8 < t' < 8$ but the average rate of occurrence determined from Eq. (19) is $\nu \sim 1/(5t')$. The event repeats at an average rate of $5t'$. This value is relatively constant over all tests and indicates that the measurable signal is composed of overlapping events (or shots) at this average rate. Figure 9 gives an alternate view of the data used to produce the ω–k chart in Fig. 8. The propagation speed is identified by the direct evaluation of the wave front slope according to $U_p = \mathrm{d}x/\mathrm{d}t$. For frequencies less than $Sr_L \sim 1$, propagation speed is best evaluated using Fig. 9. For frequencies greater than $Sr_L \sim 1$, propagation speed is best evaluated using Fig. 8. Clearly the energetic features correspond to the well known acoustic feedback loop. Downstream turbulent convection at $U_p \sim 0.6U$ grows, saturates into turbulence, and impacts the rear wall. This produces noise propagating upstream at $U_p = -a$. Upon reaching the upstream wall, the next cycle is initiated. The dominant upstream propagation evidently occurs in the quiescent environment beneath the shear layer because the propagation speed is $U_p = -a$.

Further details can be gleaned by restricting the fluctuations to the frequency regions identified in Fig. 8. This is similar to performing a POD based reconstruction on isolated Rossiter modes [10]. The result is shown on Fig. 10. Region 1 (part a) supports the basic instability but provides evidence of a three cell standing wave pattern. The cell length is equal to the cavity width linking the cells to the fundamental cross mode. Part b is associated with region 2 and identifies the higher harmonic structure that travels along with the basic instability. Part c shows the small scale structure in region 3. These ripples are consistent with the high frequency standing wave structure identified on Fig. 8. The phase velocity ω/k implied by the slope of these ripples is negative and several times greater than the speed of sound. It is an artificial parameter, resolved by recalling that energy propagates at the group velocity. By previous inference the ripples are related to the cross-stream mode through the spike at 4.5 kHz ($Sr_L = 3.5$). This is further evidence connecting the fundamental cross-stream mode with the high frequency–low wavenumber mode. It may be the key to control of the fluctuation levels by high frequency forcing [6].

Figure 11 identifies the structural changes when the leading edge is modified using devices designed to increase the thickness of the initial shear layer. This figure pertains to the sawtooth fence. The results for the ramps or the air injection show similar structure. It is well known that these devices reduce the overall fluctuation level within the cavity principally by reducing the amplitude of the tonal components evident on Fig. 5. Comparing Fig. 11 to Fig. 9 shows the expected reduction in amplitude. However, the basic structural mechanism appears unchanged. The downstream turbulent convection and the resulting upstream noise appear to propagate at similar speeds and have similar phase structure. Closer inspection indicates that the high frequency standing wave near the aft wall is still present. These observations suggest that although the fluctuation amplitude is affected by the fence, the underlying mechanism is *not*

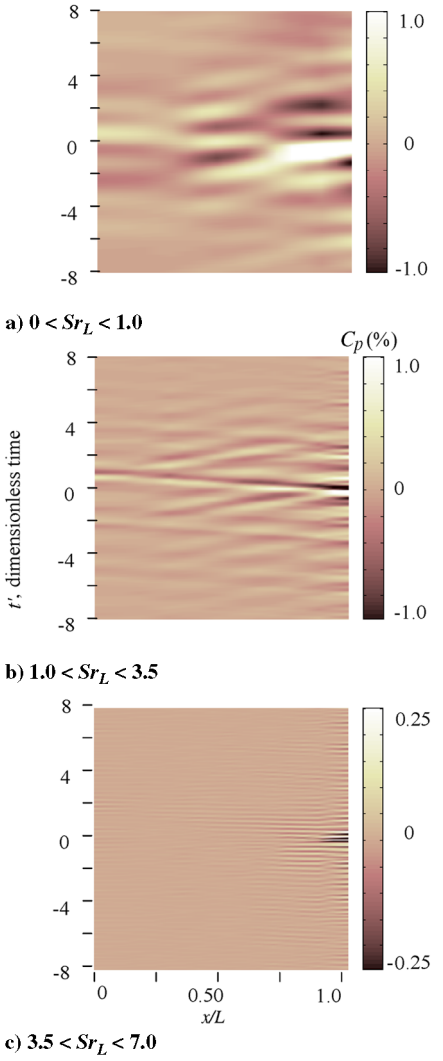

Fig. 10 *x*–*t* **event;** $M = 0.85$, $d = 41$ **mm, clean LE.**

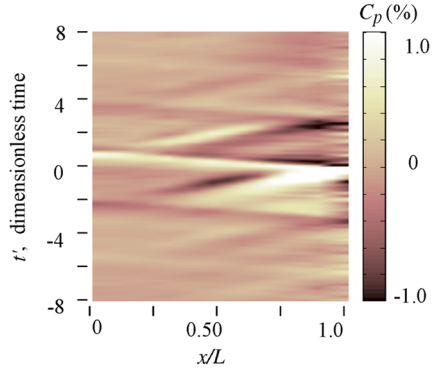

Fig. 9 *x*–*t* **event;** $M = 0.85$, $d = 41$ **mm, clean LE.**

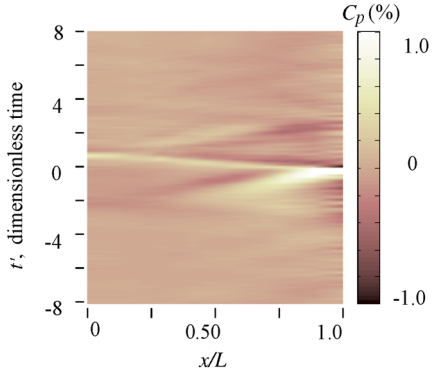

Fig. 11 *x*–*t* **event;** $M = 0.85$, $d = 41$ **mm, sawtooth LE.**

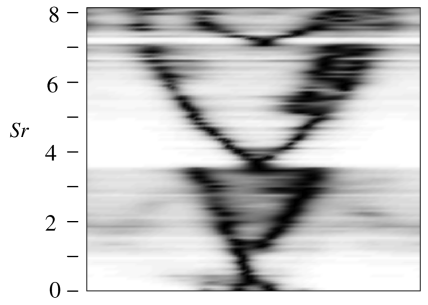

a) forward

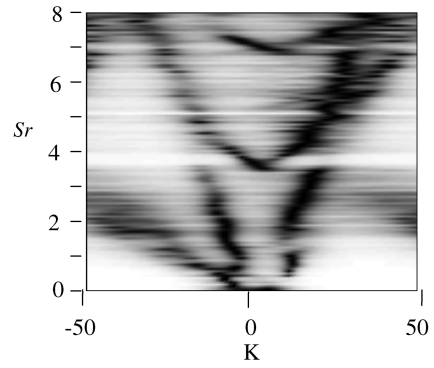

b) rear

Fig. 12 ω–k spectrum; $M = 0.85$, $d = 41$ mm, sawtooth LE.

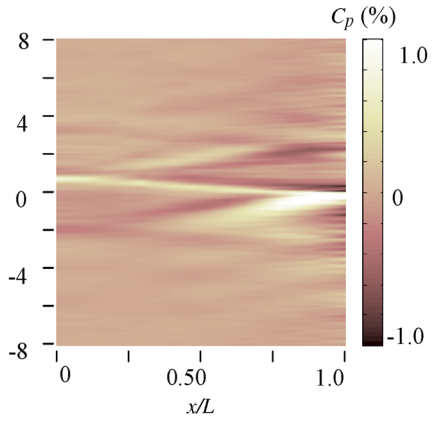

Fig. 13 x–t event; $M = 0.95$, $d = 41$ mm, sawtooth LE.

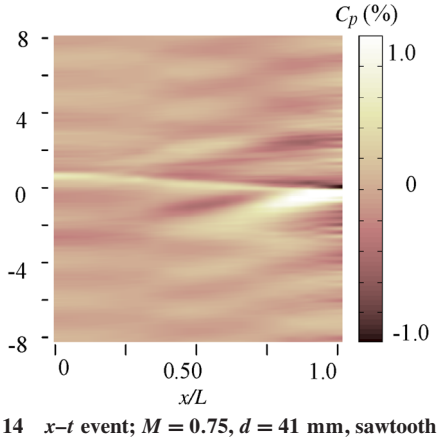

Fig. 14 x–t event; $M = 0.75$, $d = 41$ mm, sawtooth LE.

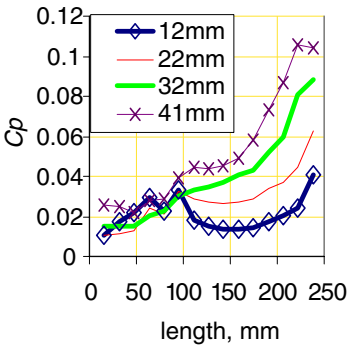

Fig. 15 Static pressure distribution along cavity floor; $M = 0.85$, clean LE.

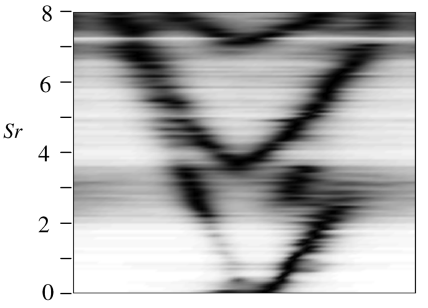

a) depth = 32 mm

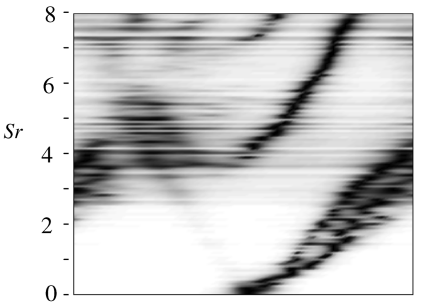

b) depth = 22 mm

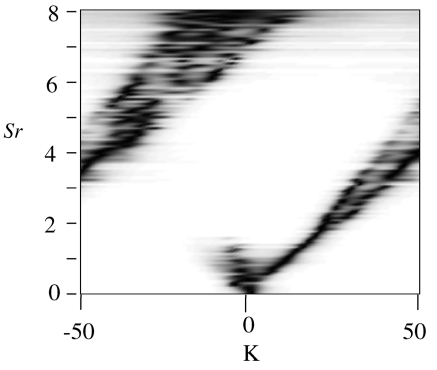

c) depth = 12 mm

Fig. 16 ω–k spectrum; $M = 0.85$, clean LE.

dependent on the shear layer conditions. Further evidence supporting this observation is shown on Fig. 12. Comparison of this ω–k plot for the sawtooth fence to the clean LE (Fig. 9) reveals essentially the same structural pattern. The principal difference is that the strength of the upstream components (feedback part of the cycle) has diminished.

Variation in flow speed over the range $0.75 < M < 0.95$ produces expected changes in the downstream turbulent convection speed but

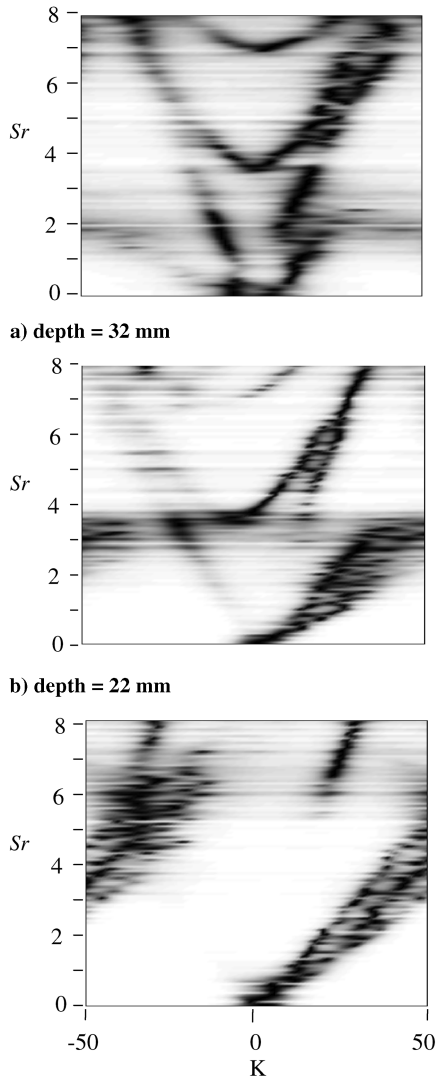

a) depth = 32 mm

b) depth = 22 mm

c) depth = 12 mm

Fig. 17 ω–k spectrum; $M = 0.85$, sawtooth LE.

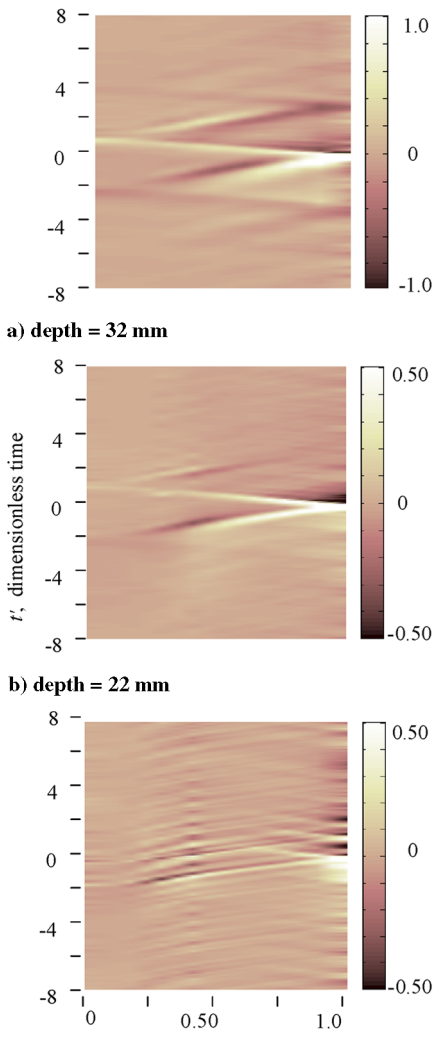

a) depth = 32 mm

b) depth = 22 mm

c) depth = 12 mm

Fig. 18 x–t event; $M = 0.85$, clean LE.

no significant change in the basic mechanism. The sequence of changes can be seen by comparing Figs. 11, 13, and 14. Detailed examination of the wave front slope identifies the propagation speeds. Higher flow speeds increase the convection speed and lower flow speeds decrease the convection speed of the turbulence. The upstream acoustic propagation does not change with flow speed because the feedback occurs below the shear layer where the flow speed is essentially zero. The high frequency standing wave is present at all speeds. The similarity of these figures indicates that variation in flow speed does not have a significant effect on the flow structure.

Reducing the cavity depth produces a more significant change in the flowfield. The general behavior is shown by the static pressure on Fig. 15. The fluctuations can be divided into two zones separated at 100 mm ($x/L \sim 0.4$). The fluctuation level in the upstream zone is independent of depth. The fluctuation level in the downstream zone shows a significant increase in the amplitude of the unsteadiness as the depth increases. At the lowest depth of 12 mm there is clear evidence of a stagnation point on the cavity floor, as indicated by the rise to a distinct peak level followed by a reduction in pressure as the flow enters the downstream zone.

Variations in the wave structure are also evident as the cavity depth is decreased. Figures 16 and 17 show the progressive variation in ω–k in the rear half of the cavity for the clean leading edge and the sawtooth, respectively. These show similar results providing further evidence that the structural features are not dependent on the shear layer conditions. The four distinct regions identified for the baseline 41 mm depth are still present at 32 mm. But, the high frequency standing wave at $Sr_L > 3.5$ for smaller depths is considerably different. The downstream leg at positive K is still present at 22 mm and both upstream and downstream legs have disappeared at 12 mm. Thus, the flowfield undergoes a structural change beginning at $d \sim 27$ mm ($d/L \sim 0.10$). This is consistent with the emergence of the distinct forward and aft zones shown in Fig. 15. These features are evidently related. Note that the wave structure on Fig. 16c wraps around to negative K due to spatial aliasing. This is a direct result of the interelement transducer spacing and not a real part of the field. The only structural difference between the clean leading edge and the sawtooth fence is the presence of the small extra wave in the upper right corner of Fig. 17. This is a downstream propagating high frequency acoustic wave at $U_p = U + a$ caused by flow separation from the sawtooth fence.

Figure 18 shows the variation with depth of the x–t event for the same conditions as on Fig. 16. Figure 9 provides the chart for $d = 41$ mm. As the depth decreases, the feedback structure becomes less pronounced but retains its overall timing for depths greater than 22 mm. The events have the same upstream and downstream propagation speeds. At 12 mm depth there is a shift to a higher frequency structure and the upstream propagation is blocked at $x/L \sim 0.4$. This is the location on Fig. 15 where the static pressure reaches a local maximum and separates the upstream zone from the downstream zone.

The interpretation given to these observations is shown in Fig. 19. For deep cavities, the growing shear layer impacts the aft wall of the cavity leaving quiescent space below the shear layer in which acoustic waves can travel forward. This uninterrupted space allows

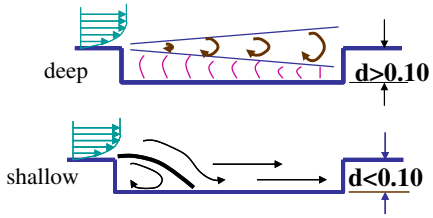

Fig. 19 Physical interpretation of cavity fluctuations.

the high frequency standing wave to exist along the entire cavity. At depths below $\sim$27 mm ($d/L < 10\%$) the growing shear layer reaches the cavity floor before impacting the aft wall. This creates a local stagnation point separating the flow into two zones: an upstream recirculation zone caused by the downstream facing step at the forward wall of the cavity, and a downstream zone caused by the flow approaching the aft wall. This stagnation point interrupts the continuity of the high frequency standing wave and prevents the strong upstream acoustic wave.

Conclusion

The unsteady pressure field in an open cavity beneath a high subsonic flow has been studied using an axial array of pressure transducers. Two array processing techniques are used to reduce the magnitude of the data processing problem to manageable levels. Both are subspace methods aimed at separating the coherent signal from the uncorrelated noise. A high frequency–low wavenumber mode has been found which is linked to the cross-stream mode of the cavity. This is superimposed on the well-known acoustic feedback loop. Leading edge devices which thicken the initial shear layer are able to reduce the overall magnitude of the fluctuations but do not change the structure of the feedback mechanism or the high frequency mode. Variation in flow speed alters the timing of the feedback mechanism but does not change the basic characteristics. Depth variation alters both the magnitude and the character of the flow structure. Deep cavities show the strongest feedback levels. As the depth is decreased, the high frequency mode becomes weaker, the feedback mechanism reduces in magnitude, and the structure becomes finer. At a critical depth $d/L \sim 0.10$ the high frequency mode disappears and the upstream feedback is cutoff at the point where the shear layer attaches to the floor.

Acknowledgements

Partial support for this work has been provided by the Air Force Arnold Engineering Development Center (AEDC) through contract no. F40600-02-C-0014. Fred Shope was the Technical Liaison. Discussion with Frank Steinle and others at AEDC served to focus the effort on the relevant practical problem of understanding weapons bay acoustics and unsteady pressures in transonic wind tunnel testing.

References

[1] Rossiter, J. E., "Wind-Tunnel Experiments on the Flow over Rectangular Cavities at Subsonic and Transonic Speeds,"Aeronautical Research Council Reports and Memoranda, No. 3438, Oct. 1964.

[2] Rockwell, D., and Naudascher, E., "Self-Sustained Oscillations of Impinging Shear Layers," *Annual Review of Fluid Mechanics*, Vol. 11, Jan. 1979, pp. 67–94.

[3] Cattefesta, L., Williams, D., Rowley, C., and Alvi, F., "Review of Active Control of Flow-Induced Cavity Resonance," AIAA 2003-3567, June 2003.

[4] Willmarth, W., and Wooldridge, C., "Measurement of the Fluctuating Pressure at the Wall Beneath a Thick Turbulent Boundary Layer," *Journal of Fluid Mechanics*, Vol. 14, Oct. 1962, pp. 187–210.

[5] Serafini, J. S., "Wall Pressure Fluctuations and Pressure-Velocity Correlations in a Turbulent Boundary Layer," NASA TR R-165, Dec. 1963.

[6] Stanek, M., Raman, G., Kibens, V., Ross, J., Odedra, J., and Peto, J., "Control of Cavity Resonance Through Very High Frequency Forcing," AIAA 2000-1905, June 2000.

[7] Forestier, N., Geffroy, P., and Jacquin, L., "The Mixing Layer over a Deep Cavity at High Subsonic Speed," *Journal of Fluid Mechanics*, Vol. 475, 25 Jan. 2003, pp. 101–145.

[8] Lumley, J. L., *Stochastic Tools in Turbulence*, Academic Press, New York, 1970.

[9] Rowley, C., Colonius, T., and Murray, R., "POD Based Models of Self-Sustained Oscillations in the Flow Past an Open Cavity," AIAA 2000-1969, Jan. 2000.

[10] Murray, N., and Ukeiley, L., "Wall-Pressure Modes in Subsonic Cavity Flows," AIAA 2005-2801, May 2005.

[11] Long, D. F., "Acoustic Source Location in Wind Tunnel Tests via Subspace Beamforming," AIAA 2003-0369, Jan. 2003.

[12] Capon, J., "High Resolution Frequency-Wavenumber Spectrum Analysis," *Proceedings of the Institute of Electrical and Electronics Engineers*, Vol. 57, No. 8, Aug. 1969, 1408–1418.

[13] Johnson, D. H., "The Application of Spectral Estimation Methods to Bearing Estimation Problems," *Proceedings of the Institute of Electrical and Electronics Engineers*, Vol. 70, No. 9, Sept. 1982, 1018–1028.

[14] Loeve, M., *Probability Theory*, 4th ed., Springer–Verlag, New York, 1978.

[15] Pisarenko, V., "The Retrieval of Harmonics from a Covariance Function," *Geophysical Journal of the Royal Astronomical Society*, Vol. 33 1973, pp. 347–366.

[16] Rice, S., "Mathematical Analysis of Random Noise," in "Selected Papers on Noise and Stochastic Processes," edited by Wax, N., Dover, New York, 1954, pp. 133–295.

J. Gore
Associate Editor